scientific reports

Check for updates

Investigation of the functional hot-spot residues of an enzyme by real-time monitoring of the enzymatic reaction using NMR and computational approaches

Toshihiko Sugiki[1,2,12]✉, Tomoki Yoshida[2,12], Masaki Tsukamoto[3], Koichiro Miyanishi[4,5], Akinori Kagawa[5,6], Natsuko Miura[7], Tomoto Ura[8,9], Jun Fukazawa[1,5], Yuko Hatanaka[5], Tsuyoshi Murata[10], Toshimichi Fujiwara[1,5], Masahiro Kitagawa[4,5], Yasushi Morita[10], Kumiko Sakai-Kato[2], Yoichi Takakusagi[8,11], Nobutada Tanaka[2] & Makoto Negoro[5,6,8]

Favipiravir is an anti-influenza prodrug that is metabolized to its phosphoribosylated form, favipiravir-ribofuranosyl-5′-monophosphate (favipiravir-RMP), by human endogenous enzyme hypoxanthine-guanine phosphoribosyltransferase (HGPRT). This enzymatic reaction is the rate-determining step in generating the active form of favipiravir, making it important to understand the molecular mechanisms underlying the HGPRT-catalyzed RMP-modification of favipiravir. However, the pharmacokinetics of this reaction have not been fully elucidated, despite X-ray crystallographic studies on the HGPRT-favipiravir complex. Here, we identified functional hot-spot residues in HGPRT that play important roles in the enzymatic conversion of favipiravir to favipiravir-RMP. Real-time monitoring of the HGPRT reaction via ligand-observed solution NMR experiments, biochemical mutagenesis of HGPRT, and computational calculations and molecular dynamics simulations, allowed us to investigate the free binding energetics and structural properties of the interaction between HGPRT and favipiravir-RMP. This powerful hybrid experimental strategy allows the identification of functional hot-spot residues in the enzyme and provide complementary structural biological information. This approach could be universally applicable to investigating drug-protein interaction modes.

Keywords Avigan, SARS-CoV-2, HGPRT, Fluorine-19, Molecular dynamics simulation

Abbreviations

HGPRT	Hypoxanthine-guanine phosphoribosyltransferase
MD	Molecular dynamics
NMPs	Nucleoside monophosphates
PRib-PP	5-phospho-α-D-ribose diphosphate

[1]Institute for Protein Research, The University of Osaka, 3-2 Yamadaoka, Suita, Osaka 565-0871, Japan. [2]Graduate School of Pharmaceutical Science, Kitasato University, 5-9-1 Shirokane, Minato-ku, Tokyo 108-8641, Japan. [3]Graduate School of Informatics, Nagoya University, Furo-cho, Chikusa, Nagoya, Aichi 464-8601, Japan. [4]Graduate School of Engineering Science, The University of Osaka, 1-3 Machikaneyama, Toyonaka, Osaka 560-8531, Japan. [5]Center for Quantum Information and Quantum Biology (QIQB), The University of Osaka, 1-2 Machikaneyama, Toyonaka, Osaka 560-0043, Japan. [6]WPI Premium Research Institute for Human Metaverse Medicine (WPI-PRIMe), The University of Osaka, 2-2 Yamadaoka, Suita, Osaka 565-0871, Japan. [7]Graduate School of Agriculture, Osaka Metropolitan University, 1-1 Gakuen-cho, Naka-ku, Sakai, Osaka 599-8531, Japan. [8]Institute for Quantum Life Science, National Institutes for Quantum Science and Technology (QST), 4-9-1 Anagawa, Inage-ku, Chiba 263-8555, Japan. [9]Institute of Pure and Applied Sciences, University of Tsukuba, 1-1-1 Tennodai, Tsukuba, Ibaraki 305–8573, Japan. [10]Department of Applied Chemistry, Faculty of Engineering, Aichi Institute of Technology, 1247 Yachigusa, Yakusa, Toyota, Aichi 470-0392, Japan. [11]Center of Quantum Life Science for Structural Therapeutics (cQUEST), Chiba University, 1-33 Yayoi-cho, Inage-ku, Chiba 263-8522, Japan. [12]Toshihiko Sugiki and Tomoki Yoshida contributed equally to this work. ✉email: sugiki.toshihiko@kitasato-u.ac.jp

RdRp	RNA-dependent RNA polymerase
RMP	Ribofuranosyl-5′-monophosphate
RTP	Ribofuranosyl-5′-triphosphate
RMSDs	Root mean square deviations
SARS-CoV-2	Severe acute respiratory syndrome coronavirus-2

Several antiviral drugs have recently been marketed, including inhibitors of viral neuraminidase of type-A and -B influenza viruses, such as Tamiflu (oseltamivir)[1,2], and viral M2 protein blockers of type-A influenza such as Symmetrel (amantadine)[3,4]. A pyrazinecarboxamide derivative, favipiravir, whose brand name is Avigan, is a prodrug. Its metabolism by endogenous enzymes in host cells converts it to an active anti-influenza compound. First, favipiravir is absorbed into host cells and phosphoribosylated into favipiravir-ribofuranosyl-5′-monophosphate (favipiravir-RMP) by hypoxanthine-guanine phosphoribosyltransferase (HGPRT) (Figure S1)[5–7]. Next, favipiravir-RMP is further metabolized to its ribofuranosyl-5′-triphosphate form (favipiravir-RTP) by other various enzymes (Figure S1). Since it would attenuate replication of the viral RNA-genome of, for example, influenza and SARS-CoV-2[5,8–15], favipiravir is expected as one of the hopeful candidates to concur pandemic outbreak of viral infectious diseases of the coming future.

Because the first step of the enzymatic reaction catalyzed by HGPRT is the rate-determining in generating favipiravir-RTP, efficiency of this enzymatic conversion from favipiravir to favipiravir-RMP by HGPRT directly influences the intracellular amount of favipiravir-RTP[6,7]. It means that elucidating molecular mechanisms by which HGPRT catalyzes the modification of favipiravir is important for characterizing its pharmacokinetics and for developing next-generation-favipiravir-analogues exhibiting enhanced anti-viral activity.

A previous X-ray crystallographic analysis of the HGPRT complexed with favipiravir-RMP indicated that the HGPRT amino acid residues K68, T138, K140, K165, and D193 form a binding pocket for favipiravir-RMP[6] (Fig. 1). However, which of those residues play functional roles in the enzymatic modification of favipiravir remain unknown.

By taking advantage of the fact that one fluorine atom (^{19}F) is natively existing in one favipiravir molecule, we recently developed an analytical method allowing the direct and real-time observation of the HGPRT-catalyzed conversion of favipiravir to favipiravir-RMP by utilizing solution ^{19}F-NMR spectroscopy[16–19]. This method allows direct observation of the target reaction, without using isotope-label samples and complicating background signals. Here, we determined the functional hot-spots of HGPRT by NMR real-time ligand-observations and computational approaches.

Materials and methods

Materials

This study was supported by FUJIFILM Toyama Chemical Co., Ltd., which kindly prepared and provided favipiravir for our use. Other materials were purchased from Sigma-Aldrich and Nacalai Tesque.

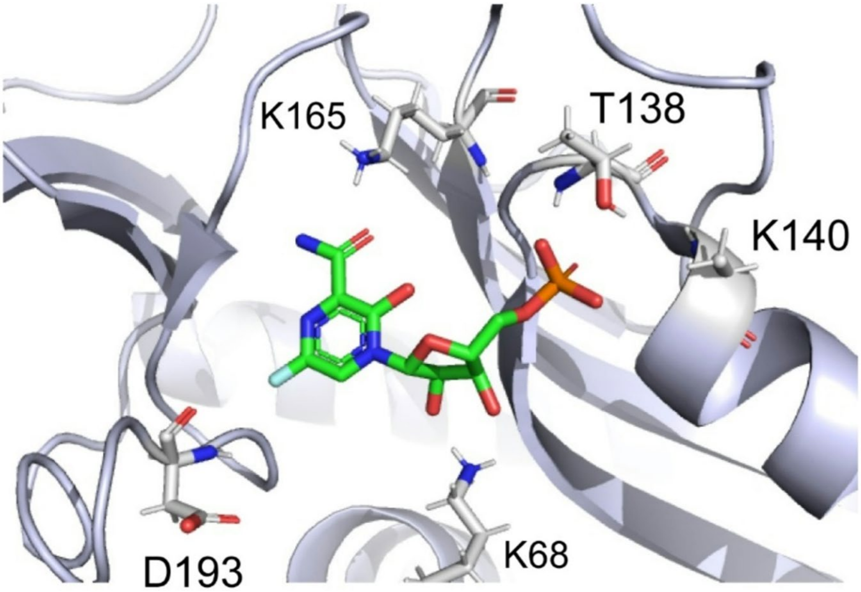

Fig. 1. The locations of key amino acid residues were denoted on the crystal structure of the complex between human hypoxanthine-guanine phosphoribosyltransferase (HGPRT) (shown as a silver ribbon model) and favipiravir-ribofuranosyl-5′-monophosphate (favipiravir-RMP) (PDB ID 4KN6, shown as a stick model). Hydrogen atoms have been added in their riding positions.

Sample preparation

The cDNA encoding human HGPRT single mutants, T138A, K140M, and D193N, were prepared using a QuikChange Site-Directed Mutagenesis Kit (STRATAGENE). The corresponding recombinant proteins (amino acid residues 1-218) were prepared using an *Escherichia coli* expression system and purified by column chromatography, as previously described[19]. The single-site mutants T138A, K140M, and D193N were designed based on prior crystallographic analyses[6], which identified these residues as part of the favipiravir-RMP binding pocket. The mutations were chosen to selectively alter side-chain physicochemical properties (removal of hydroxyl, loss of positive charge, or neutralization of carboxylate) while preserving overall structural integrity, thereby enabling functional evaluation of each residue.

Enzymatic RMP-modification of favipiravir by HGPRT

The enzymatic reaction pre-mix solution comprised 10 mM favipiravir, 10 mM *P*Rib-*PP*, 10 mM $MgCl_2$, 1 mM ethylene glycol-bis(2-aminoethylether)-*N*,*N*,*N′*,*N′*-tetraacetic acid (EGTA), and 5%[v/v] ^2H_2O in phosphate-buffered saline (PBS), as described previously[19].

Solution NMR experiments

All ^{19}F- and ^{31}P-NMR experiments were performed using a Bruker AVANCE III 400-MHz NMR spectrometer equipped with a room-temperature broad-band fluorine observation (BBFO) probe, or a Bruker AVANCE III 500-MHz instrument equipped with a cryogenic broad-band observation (BBO) probe, respectively, at a sample temperature of 298 K. Following mixing recombinant HGPRT protein to the reaction pre-mix to be 0.5 μM of the final protein concentration, one-dimensional (1D) ^{19}F- or ^{31}P-NMR data collection was promptly started as previously described[19]. The NMR data were analyzed using the TopSpin 3.6.2 (Bruker) and Mnova (MestReNova) software. The V_{max} and K_m values were determined by Michaelis-Menten analysis using the ICEKAT software[19,20]. The k_{cat} values were also calculated from the V_{max} values and the concentration of HGPRT protein (0.5 μM).

Computational analyses of binding free energy and enzyme kinetics

Differences in the enzymatic parameters (K_m and k_{cat}) for the conversion of favipiravir to favipiravir-RMP catalyzed by wild-type and mutant HGPRT were determined by computational calculations of the binding free energy (ΔG), and by molecular dynamics (MD) simulations. The dissociation of nucleoside monophosphates (NMPs) is the rate-limiting step in HGPRT-catalyzed reactions[21,22], and thus the dissociation of favipiravir-RMP from HGPRT is the major rate-limiting step for generation of favipiravir-RTP. Since ΔG reflects binding affinity, which is expected to correlate with differences in K_m, differences in K_m values for wild-type and mutant HGPRT estimated by NMR experiments were assessed by calculating ΔG values for favipiravir-RMP binding to each HGPRT variant. Given that NMP dissociation is the rate-limiting step, differences in k_{cat} values were assessed by analyzing the dynamic stability of the enzyme–ligand complexes through molecular dynamics (MD) simulations, under the assumption that more stable complexes may exhibit slower product release, as reflected in the observed k_{cat} values.

Preparation of virtual HGPRT–favipiravir-RMP complex structural models

The structures of HGPRT (wild-type, T138A, K140M, and D193N) complexed with favipiravir-RMP were constructed virtually using the X-ray crystal structure of the wild-type HGPRT–favipiravir-RMP complex (PDB ID: 4KN6, chain A). The missing N-terminal amino acid residues were created using PDBFixer, a module in the OpenMM molecular dynamics framework[23]. The missing residues corresponding to the amino acids 103–122 were reconstructed by superimposing the HGPRT structure from the GMP-bound X-ray crystal structure (PDB ID: 1HMP) onto the 4KN6 structure based on the Cα atoms using PyMOL[24], and then residues 100–126 amino acids of 4KN6 were replaced with the corresponding 1HMP residues to ensure structural continuity of the flexible loop region, including neighboring residues adjacent to the missing segment. The protein structures were then preprocessed using the Protein Preparation Wizard in Schrödinger Suite 2023-4[25,26], involving the addition of hydrogen atoms and assignment of tautomeric and protonation states. Protonation states of ionizable residues (such as Asp, Glu, His, Lys, and Arg) were determined using the pK_a prediction algorithm implemented in the Protein Preparation Wizard, at a target pH of 7.4 ± 2.0, and were used consistently in all subsequent simulations. The default settings predicted Glu133 to be neutral, but this residue was manually set to the deprotonated state to reflect its salt-bridge interaction with the nearby positively charged Lys68. Energy minimization was then performed using the OPLS_2005 force field (converged to an RMSD of 0.3 Å for heavy atoms). Point mutations were introduced using PyMOL[24] to generate the mutant complex structures.

The MM-GBSA calculations

Molecular mechanics with generalized Born and surface area solvation (MM-GBSA) calculations of the four prepared complex structures (wild-type, T138A, K140M, and D193N) were performed using Prime in Schrödinger Suite 2023-4[27–29] and the OPLS_2005 force field to estimate the ΔG values in aqueous solution. The ΔG values in aqueous solution were determined by subtracting the total free energy of the isolated protein and ligand from that of the solvated complex, during which the ligand and protein side chains within 4 Å of the ligand (including mutation sites) were optimized to accommodate conformational changes induced by the mutations.

We note that the MM-GBSA binding free energy values reported in Table 3 were obtained from the minimized structural models of each HGPRT–favipiravir-RMP complex, not from snapshots of the MD trajectories. Thus, our ΔG values represent static estimates based on energy-minimized complexes, rather than dynamic averages. This protocol was chosen to provide a consistent and computationally tractable comparison among variants, while the MD trajectories were analyzed separately to assess dynamic stability (RMSD, hydrogen bonding, and hydrophobic contacts).

Experimental binding free energies (ΔG_{exp}) were also estimated from the K_m values obtained in the enzyme kinetics experiments (Table 2), using the relation $\Delta G_{exp} = RT \ln K_m$, with $R = 1.987$ cal mol^{-1} K^{-1} and T = 298 K. These values were compared with the MM-GBSA binding free energies (Table S3).

Molecular dynamics simulations

Molecular dynamics (MD) simulations were conducted using Desmond in Schrödinger Suite 2019-1[30,31] for the four complexes (wild-type, T138A, K140M and D193N) obtained from the MM-GBSA calculations. Each complex was placed in a cubic box with at least 10 Å between the protein and the box edge, solvated with water (SPC model), and neutralized by adding Na^+ counterions. No additional bulk salt was added, corresponding to an effective ionic strength of approximately 0 mM. The OPLS_2005 force field was applied to both protein and ligand, long-range electrostatics were treated with the particle mesh Ewald (PME) method, and covalent bonds involving hydrogens were constrained using the SHAKE algorithm. The MD simulations were performed under NPT (isothermal-isobaric) ensemble conditions, with a temperature of 300 K and a pressure of 1.01325 bar. Prior to production, each system was equilibrated using Desmond's standard relaxation protocol, consisting of a series of short Brownian dynamics and NVT/NPT steps with gradually released restraints on solute heavy atoms. Production simulations were then continued for 50 ns, and simulation trajectories were recorded every 50 ps, yielding a total of 1000 frames. Eight independent 50-ns MD simulations were performed for each complex under the same NPT conditions, using different random seeds to enhance statistical reliability. Rather than running a few long trajectories, we employed multiple short, independent replicas to increase pathway diversity across different velocity seeds and to capture rare dissociation-like events, while keeping conditions identical for robust relative comparisons.

Differences in dynamic behavior between the complexes were quantitatively evaluated by calculating the root mean square deviations (RMSDs) of both the ligand and protein relative to the initial structure from the production run. The time evolution of hydrogen bonding interactions between the ligand and protein was also analyzed to assess binding stability and interaction patterns. Trajectories were analyzed using the MDAnalysis package[32,33]. Hydrogen bonds were identified using the HydrogenBondAnalysis module of MDAnalysis, defining nitrogen and oxygen atoms as donors or acceptors. Hydrogen bonding criteria were set as a donor-acceptor distance cutoff of 3.5 Å and a donor-hydrogen-acceptor angle cutoff of 135°. Hydrophobic contacts were identified when the distance between the ligand and the carbon atoms of hydrophobic residues was ≤ 3.6 Å.

Results

Solution NMR and mutagenesis experiments to investigate the activity of the favipiravir-RMP modification reaction by HGPRT

The desired enzymatic reaction catalyzed by HGPRT shown in Figure S1, can be reconstructed in vitro by using 5-phospho-α-D-ribose diphosphate (*P*Rib-*PP*) as monophospho-D-ribose donor (Figure S2)[6,19]. The enzymatic conversion of favipiravir to favipiravir-RMP by the HGPRT wild-type or by its T138A, K140M, and D193N mutants, those amino acid residues form a favipiravir-RMP binding site (Fig. 1), were investigated by performing real-time ligand-observed one-dimensional (1D) ^{19}F-NMR experiments (Fig. 2). We could not study this conversion by the K68 and K165 mutants, even though these residues located near the favipiravir-RMP binding site (Fig. 1) because these recombinant HGPRT proteins were not expressed.

Individual 1D ^{19}F-NMR spectra (1 min) were collected at 5 min intervals for 12 h[19], then the resulting 144 of the 1D ^{19}F-NMR spectra were stacked to show time-dependent alteration of each NMR spectrum (the left panels in Fig. 2A and D). The red and yellow asterisks in the left panel of Fig. 2A show that the single ^{19}F-NMR peaks derived from favipiravir and favipiravir-RMP were separately observed at − 94.7 and − 96.2 ppm, respectively, and were unambiguously assigned by referring a previous report[19]. A time-dependent attenuation was observed in the ^{19}F-NMR peak at − 94.7 ppm, derived from favipiravir when catalyzed by HGPRT wild-type, T138A, or K140M (Fig. 2A and C, the left panels). In parallel, a single new ^{19}F-NMR peak appeared at − 96.2 ppm and its signal intensity was gradually increased in a time-dependent manner (Fig. 2A and C, the left panels).

We estimated the concentrations of favipiravir and favipiravir-RMP based on the integral values of these 1D ^{19}F-NMR signals. Plotting these concentrations against elapsed time (Fig. 2A and C, the right panels), we determined the initial rates of enzymatic conversion (V_0, μM/min) of favipiravir to favipiravir-RMP catalyzed by each HGPRT (Table 1). The V_0 values of the decrease in favipiravir concentration and the increase in favipiravir-RMP concentration catalyzed by HGPRT wild-type were 5.34 ± 0.13 and 6.74 ± 0.13 μM/min, respectively (Fig. 2A; Table 1). The V_0 values of the decrease in favipiravir concentration and the increase in favipiravir-RMP concentration catalyzed by HGPRT T138A were 34.5 ± 2.93 and 40.9 ± 2.13 μM/min, respectively (Fig. 2B; Table 1). Thus, the initial reaction rate catalyzed by HGPRT was increased approximately six times by substituting T138 residue in the HGPRT to an alanine. The V_0 values of the decrease in favipiravir concentration and the increasing favipiravir-RMP concentration catalyzed by HGPRT K140M were 5.65 ± 0.15 and 6.44 ± 0.08 μM/min, respectively (Fig. 2C; Table 1), showing that the initial reaction rate was not severely affected by the substitution of K140 residue in the HGPRT with methionine. Interestingly, only one ^{19}F-NMR peak was observed at − 94.7 ppm when HGPRT D193N was used (Fig. 2D), and time-dependent alterations in that peak were not occurred (Fig. 2D; Table 1), suggesting that this HGPRT mutant exhibits no enzymatic activity for the conversion of favipiravir to favipiravir-RMP.

The V_0 values at various concentrations of favipiravir (1, 3, 5, 7, and 10 mM) were examined similarly to provide the substrate (favipiravir)-dose-dependent V_0 values (Figure S3 and Table S1). The favipiravir-concentration-dependent V_0 values were fit with the Michaelis-Menten equation to determine the general enzymatic kinetic parameters, such as V_{max}, K_m, and k_{cat} of the HGPRT wild-type, T138A, and K140M enzymes

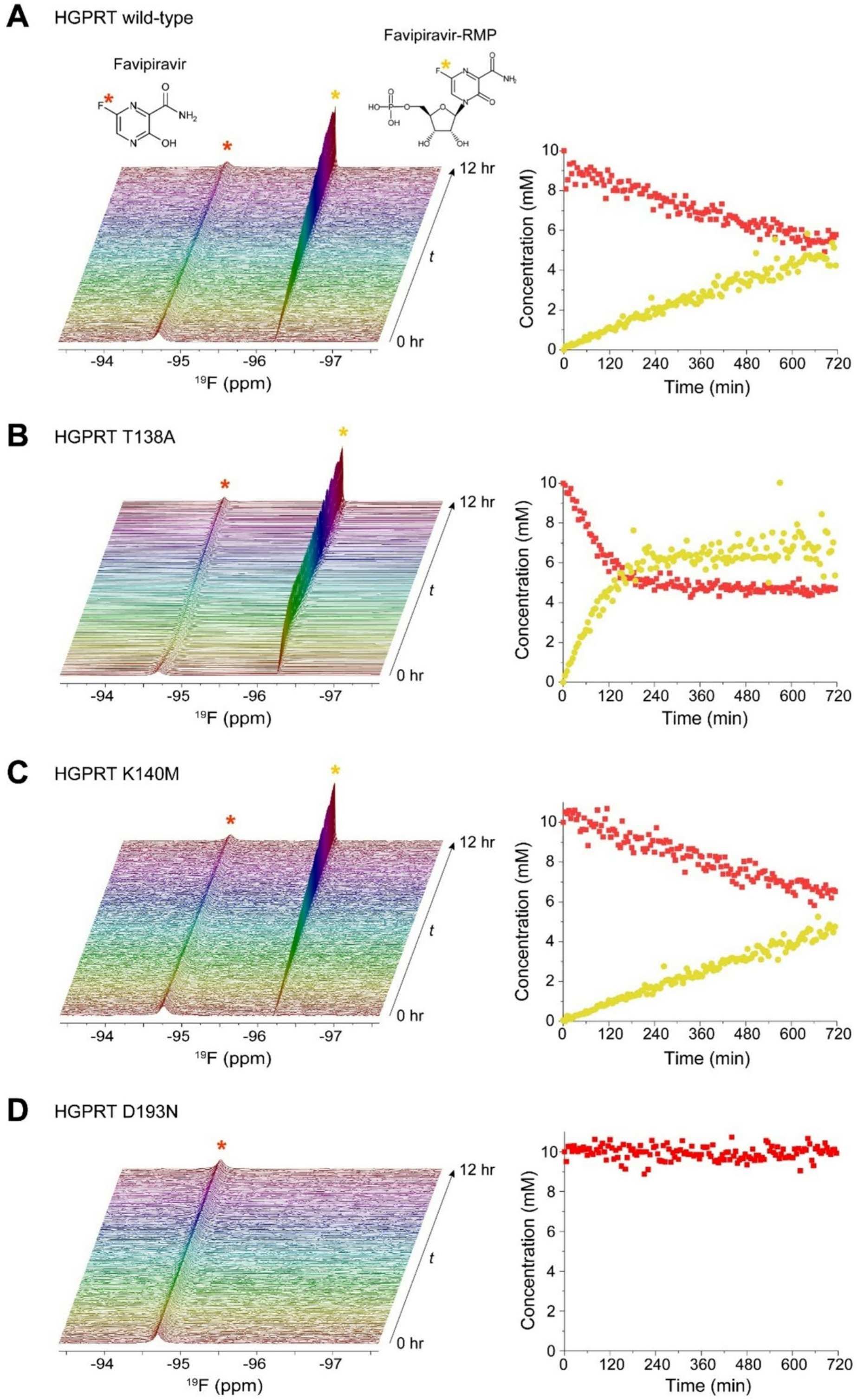

Fig. 2. Real-time observation of the HGPRT-catalyzed conversion of favipiravir to favipiravir-RMP, based on time-lapse one-dimensional (1D) ^{19}F-NMR data collection (**A–D**). The ^{19}F-NMR spectra show time-dependent changes due to the conversion of favipiravir to favipiravir-RMP, catalyzed by HGPRT wild-type (**A**), HGPRT T138A (**B**), HGPRT K140M (**C**), and HGPRT D193N (**D**). The ^{19}F-NMR spectra are represented in a time-dependent stacked style (left panels, 144 spectra were collected over 12 h). The red and yellow asterisks denoted on the stacked ^{19}F-NMR spectra indicate ^{19}F-NMR signals assigned to favipiravir and favipiravir-RMP fluorine atoms, respectively. The phosphate esters of favipiravir and favipiravir-RMP (drawn in Panel **A**) are shown in the acid form for simplicity. The concentrations of favipiravir and favipiravir-RMP were estimated from the integral values of their ^{19}F-NMR signals, and their time-dependent changes are plotted versus time (the right panels). The initial rates of the HGPRT-catalyzed conversion of favipiravir to favipiravir-RMP (V_0, μM/min) were calculated from these plots and are tabulated in Table 1.

HGPRT	Wild-type	T138A	K140M	D193N
Favipiravir	5.34 ± 0.13	34.5 ± 2.93	5.65 ± 0.15	0
Favipiravir-RMP	6.74 ± 0.13	40.9 ± 2.13	6.44 ± 0.08	(not observed)

Table 1. Initial reaction rates (V_0, μM/min)* of the conversion of favipiravir to favipiravir-RMP by wild-type HGPRT and its point mutants, T138A, K140M, and D193N. *These V_0 values were calculated from the ^{19}F-NMR data shown in Fig. 2.

HGPRT	Wild-type	T138A	K140M
V_{max} (μM/min)**	18.5 ± 1.58	74.1 ± 12.1	10.7 ± 0.41
K_m (mM)**	22.6 ± 2.35	10.7 ± 2.65	9.44 ± 0.54
k_{cat} (min^{-1})	37.0 ± 3.16	148 ± 24.2	18.9 ± 1.07

Table 2. Kinetic parameters** of the enzymatic conversion of favipiravir to favipiravir-RMP by wild-type HGPRT and its point mutants (T138A and K140M)***. **These parameters were determined by fitting the V_0 values at various favipiravir concentrations (Table S1) to the Michaelis-Menten equation. ***These parameters for HGPRT D193N could not be estimated because that protein has no enzymatic activity (as shown in Fig. 2; Table 1).

HGPRT	Wild-type	T138A	K140M	D193N
ΔG (kcal/mol)	− 31.16	− 34.49	− 30.62	− 33.99

Table 3. Binding free energy (ΔG) between HGPRT and favipiravir-RMP.

(Table 2). As a result, the V_{max}, K_m, and k_{cat} values of HGPRT T138A were 74.1 ± 12.1 μM/min, 10.7 ± 2.65 mM, and 148 ± 24.2 min^{-1}, respectively (Table 2), showing an approximately 4-, 0.5-, and 4-times increase, respectively, over that of the HGPRT wild-type (Table 2).

The V_{max}, K_m, and k_{cat} values of HGPRT K140M were 10.7 ± 0.41 μM/min, 9.44 ± 0.54 mM, 18.9 ± 1.07 min^{-1}, respectively (Table 2), indicating that the V_{max} and k_{cat} values of HGPRT K140M were decreased approximately 2-times compared to that of the HGPRT wild-type (Table 2). On the other hand, the K_m value of HGPRT K140M was increased approximately 2-times compared to that of the wild-type (Table 2).

The HGPRT D193N showed no activity for conversion of favipiravir to favipiravir-RMP, and thereby its enzymatic parameters could not be determined (Fig. 2D; Table 1).

Phosphorus atoms are natively present in *P*Rib-*PP* and PP*i* molecules (Figure S2), allowing detection of the catalytic reaction by performing phosphorus (^{31}P)-NMR experiments[19,34,35]. The 1D ^{31}P-NMR spectra (30 min) were measured continuously for 12 h, resulting in 24 of sequential 1D ^{31}P-NMR spectra. The single ^{31}P-NMR signals were observed at -2.6, -3.1, and – 8.1 ppm, derived from *P*Rib-*PP* and PP*i* (Figure S4), and were unambiguously assigned as phosphorus at the β-positions of *P*Rib-*PP*, PP*i*, and at the α-positions of *P*Rib-*PP*, respectively, by referring to the previous reports[19,36]. The decrease in the ^{31}P-NMR signals of β- and α-positions of *P*Rib-*PP* and their increase in the PP*i*, analogous to the ^{19}F-NMR data mentioned above, allowed us to estimate the V_0 values of the phosphoribosylation reaction of favipiravir (Figure S4, Table S2). Similar to the previous study reported by Sugiki et al.., however, spontaneous hydrolysis of *P*Rib-*PP* made accurate analyses difficult; the intensities of the ^{31}P-NMR signals of *P*Rib-*PP* and PP*i* decreased over time in the presence or absence of the enzyme[19]. The V_0 values could not be accurately estimated from the ^{31}P-NMR data even if the V_0 values of *P*Rib-*PP* in the absence of HGPRT were subtracted from the V_0 values in the presence of HGPRT, as indicated in the Table S2 caption, to exclude the effect of the spontaneous hydrolysis of *P*Rib-*PP*[19].

Computational analyses of the mode of interaction between HGPRT and favipiravir-RMP

Table 3 presents the binding free energies, ΔG, in aqueous solution for the four structural models of favipiravir-RMP bound to HGPRT (wild-type, T138A, K140M, and D193N), estimated by MM-GBSA analyses. Consistently, the phosphate group of favipiravir-RMP was stabilized by amino acid residues 137–141, and the hydroxyl group of the sugar moiety of favipiravir-RMP was stabilized by the backbone of I135 and the side chain of K68 residues (Fig. 3). Additionally, the base moiety of favipiravir-RMP was stabilized by the backbone of V187 (Fig. 3). The MM-GBSA calculations showed that favipiravir-RMP has a higher binding affinity for HGPRT T138A compared to wild-type (Table 3). In contrast, the binding affinity of favipiravir-RMP for HGPRT K140M was estimated to be similar to that of wild-type (Table 3). The binding affinity of favipiravir-RMP for HGPRT D193N was estimated to be higher than that of wild-type (Table 3), although HGPRT D193N showed no enzymatic activity (Fig. 2; Table 2).

Figure 4 presents representative results of the MD simulation, showing the time evolution of the root mean square deviation (RMSD) values of heavy atoms of favipiravir-RMP and HGPRT, and indicating the time-

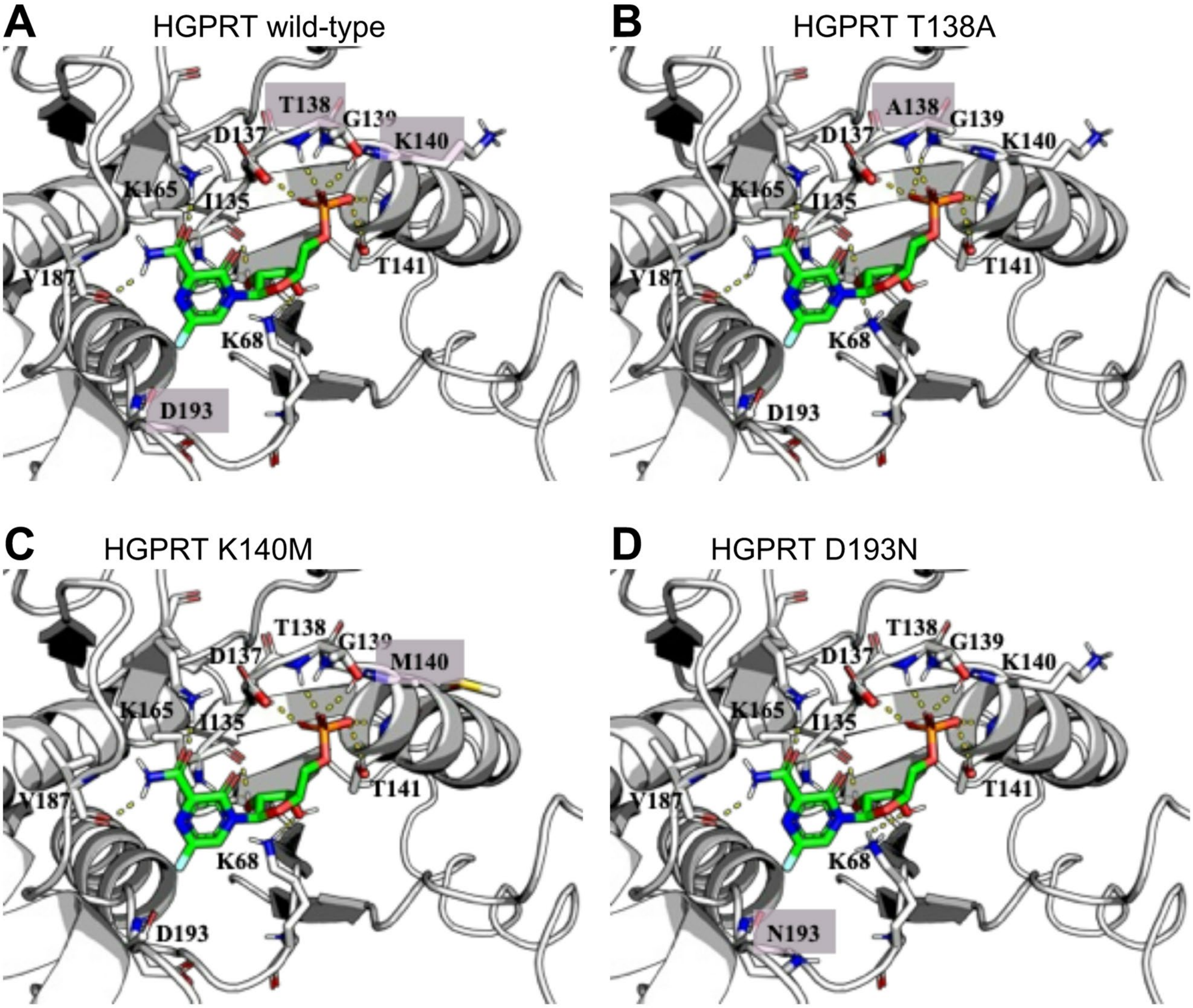

Fig. 3 . Energy-minimized structural models of the HGPRT–favipiravir-RMP complexes used for MM-GBSA binding free energy calculations (**A–D). (A**) HGPRT wild-type, (**B**) T138A, (**C**) K140M, and (**D**) D193N. The models were prepared from the crystallographic structure (PDB ID: 4KN6) and refined by energy minimization with the OPLS_2005 force field. The yellow dashed lines indicate hydrogen bonds. The structural models were visualized using PyMOL[24].

dependent spatial fluctuations of these atoms. Note that the RMSD results for D193N are not included in Fig. 4, but are provided in the Supporting Information (Figures S5–S36). Favipiravir-RMP was retained in the binding site of HGPRT wild-type, K140M, and D193N in all eight trajectories, and in seven of eight trajectories for HGPRT T138A (Figures S5–S36). Figure 4 shows representative trajectories only; the complete RMSD plots for all eight trajectories are provided in Figures S5–S36. Table 4 summarizes the statistical analyses of the RMSD fluctuations over time.

Figure 5 shows the time evolution of the number of hydrogen bonds and hydrophobic contacts between favipiravir-RMP and HGPRT in the MD simulation trajectories shown in Fig. 4. The bar graphs on the right-side inset of Fig. 5 indicate the average number of these interactions. In the case of HGPRT wild-type, the phosphate group of favipiravir-RMP primarily formed hydrogen bonds with T138 (backbone and side chain), G139 (backbone), K140 (backbone and side chain), and T141 (backbone and side chain). Additionally, the hydroxyl group of the sugar moiety of favipiravir-RMP formed hydrogen bonds with the side chain of E133 (Fig. 5A). In the case of HGPRT T138A, the phosphate group of favipiravir-RMP formed hydrogen bonds with D137 (side chain), A138 (side chain), G139 (backbone), K140 (backbone and side chain), and T141 (backbone and side chain), while the hydroxyl group of the sugar moiety of favipiravir-RMP formed hydrogen bonds with E133 (side chain) (Fig. 5B). In the case of HGPRT K140M, the phosphate group of favipiravir-RMP formed hydrogen bonds with K102 (side chain), D137 (side chain), T138 (backbone and side chain), and G139 (backbone), while the hydroxyl group of the sugar moiety of favipiravir-RMP formed hydrogen bonds with K102 (side chain) (Fig. 5C). The nucleobase also formed hydrogen bonds with the main chains of V187 and D193. Loss of the hydrogen bond with the side chain of K140 would shift the position of favipiravir-RMP closer to V187 and D193,

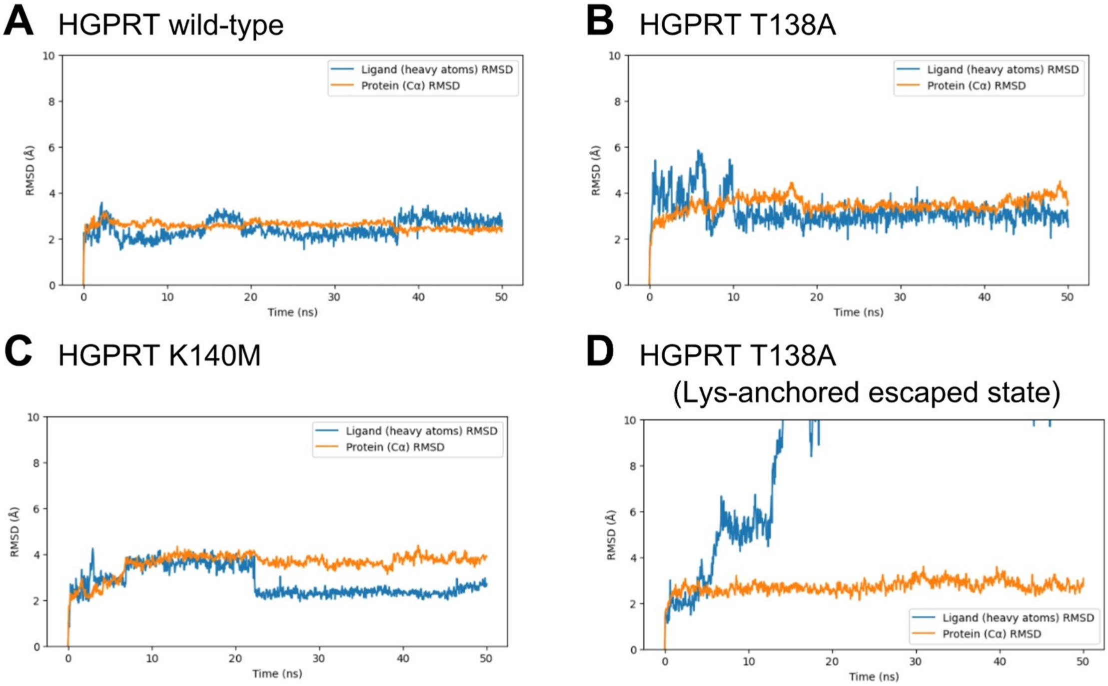

Fig. 4. Time evolution RMSD values of the favipiravir-RMP and HGPRT heavy atoms, obtained from MD simulations (**A–D**). Representative spectra of (**A**) HGPRT wild-type (Run 4), (**B**) HGPRT T138A (Run 3), (**C**) HGPRT K140M (Run 1), (**D**) HGPRT T138A (Run 1; calculated as a condition of Lys-anchored escaped state).

	Wild-type		**T138A**		**K140M**		**D193N**	
	RMSD$_{ave}$	**RMSD$_{SD}$**	**RMSD$_{ave}$**	**RMSD$_{SD}$**	**RMSD$_{ave}$**	**RMSD$_{SD}$**	**RMSD$_{ave}$**	**RMSD$_{SD}$**
Run1	3.89	0.66	11.78	5.16	2.79	0.63	4.21	0.79
Run2	2.98	0.86	3.71	0.46	4.82	1.73	3.50	0.50
Run3	3.49	0.77	3.17	0.61	4.73	1.33	4.82	0.92
Run4	2.43	0.40	4.12	1.37	4.95	1.00	4.18	0.53
Run5	4.80	0.91	3.66	0.43	3.05	0.75	4.16	0.94
Run6	4.10	0.91	3.01	1.24	3.53	0.81	4.05	1.23
Run7	4.68	0.55	2.24	0.51	4.34	0.79	3.79	0.98
Run8	4.26	0.69	4.23	0.50	4.29	0.79	3.52	0.64
Min.	2.43	0.40	2.24 (2.24)	0.43 (0.43)	2.79	0.63	3.50	0.50
Max.	4.80	0.91	11.78 (4.23)	5.16 (1.37)	4.95	1.73	4.82	1.23
Median	4.00	0.73	3.68 (3.66)	0.56 (0.51)	4.32	0.80	4.11	0.86

Table 4. Statistical analysis of the time evolution of RMSD values from the MD simulations*, **, ***. *The table presents the mean RMSD (RMSD$_{ave}$) and standard deviation (RMSD$_{SD}$) over 50 ns for each simulation run. **All values are given in Å. ***Values in parentheses were calculated after excluding the Lys-anchored escaped state. Min (minimum), Max (maximum), and Median represent the corresponding values for RMSD$_{ave}$ and RMSD$_{SD}$ across the eight MD runs.

increasing interactions between the favipiravir-RMP and these two residues. In this trajectory, the side chain of K102 interacted with the hydroxyl group of the sugar moiety of favipiravir-RMP (Fig. 5C). Figure 5D shows the trajectory by which favipiravir-RMP complexed with HGPRT T138A transitions to a "Lys-anchored escaped" state (Figure S37); favipiravir-RMP can dissociate from the binding site of HGPRT T138A while maintaining the interaction between favipiravir-RMP and the side chain of K140 residue, and this trajectory showed a new interaction between R169 side chain of HGPRT T138A and the phosphate group of favipiravir-RMP would be generated following dissociation of favipiravir-RMP from the binding site.

The ΔG_{exp} values estimated from the K_m parameters were in reasonable agreement with the MM-GBSA results in terms of relative trends among the variants (Table S3). Because K_m does not directly represent the dissociation constant (K_d) in multi-substrate enzymes such as HGPRT, exact agreement of absolute values

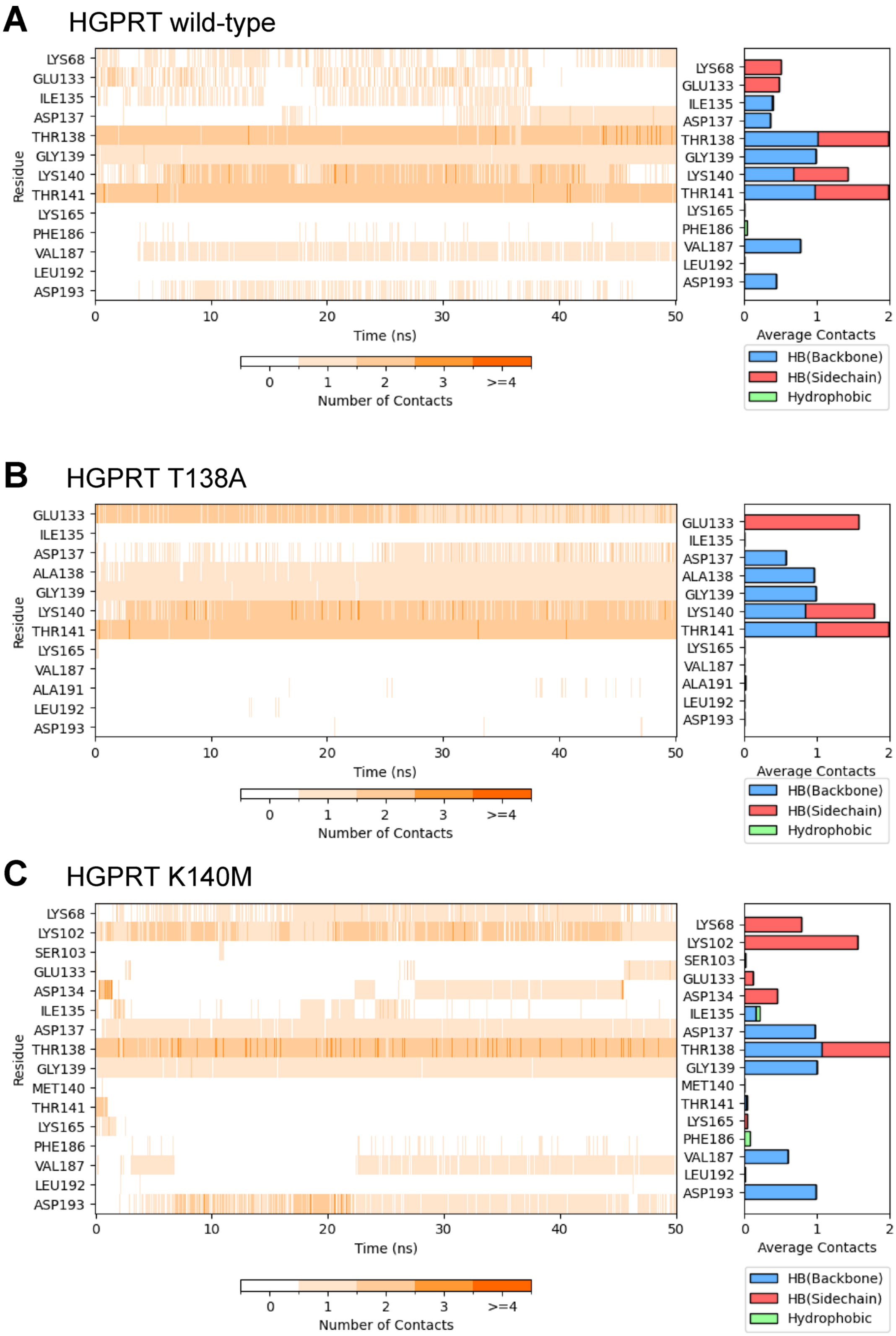

Fig. 5. Time evolution of hydrogen bonds and hydrophobic contacts between the favipiravir-RMP and HGPRT. The figures indicate the number of hydrogen bonds (involving either the backbone or side chain) and the number of hydrophobic contacts (**A**–**D**). (**A**) HGPRT wild-type (Run 4), (**B**) HGPRT T138A (Run 3), (**C**) HGPRT K140M (Run 1), (**D**) HGPRT T138A (Run 1; calculated as Lys-anchored escaped state).

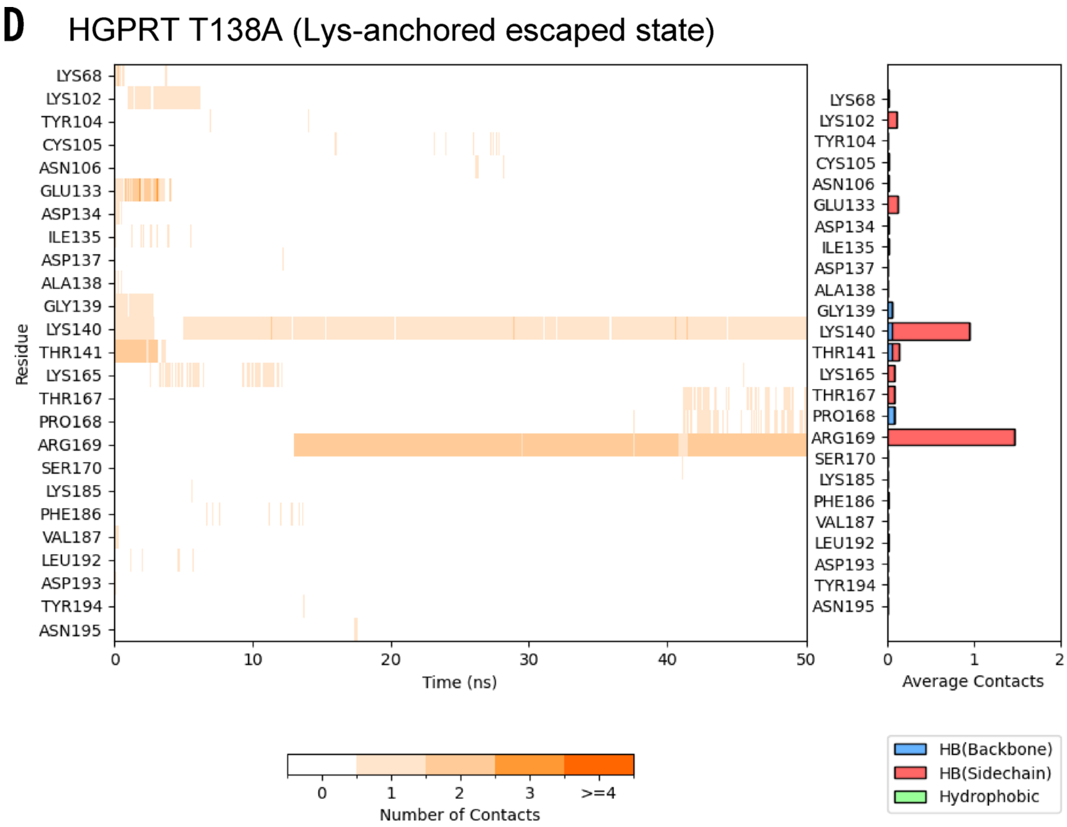

Fig. 5. (continued)

between ΔG_{exp} and computed ΔG is not expected. Nonetheless, the relative consistency supports the validity of the computational approach and may help readers to interpret the results on a thermodynamic scale.

Discussion

In our samples, only favipiravir contains a fluorine atom, and thus the two observed ^{19}F-NMR peaks are derived from favipiravir and its chemically modified analogue. The V_0 values corresponding to a decrease in favipiravir concentration and an increase in favipiravir-RMP concentration due to catalysis by HGPRT wild-type were overall consistent with a previous report[19].

The previous X-ray crystallographic analyses suggested that the backbone amide group of T138 electrostatically interacts with the phosphate group of the RMP moiety of favipiravir-RMP (Fig. 1), and further suggested that the hydroxyl group of the side chain of T138 is in close proximity to the RMP moiety of favipiravir-RMP (Fig. 1). The T138A mutation of HGPRT is identical to the removal of a hydroxyl group from the T138 side chain, and loss of the hydrogen bond between the side chain of T138 and favipiravir-RMP would decrease the structural stability of the HGPRT – favipiravir-RMP complex. On the other hand, it is interesting structural insights that the T138 residue would hinder the interaction between HGPRT and favipiravir-RMP due to the repulsive or steric effects of negative charges between the hydroxyl group of the T138 side chain and the phosphate group of RMP moiety in favipiravir-RMP. The NMR data demonstrated that favipiravir-RMP has a higher binding affinity for HGPRT T138A and K140M than the wild-type (Table 2), and MM-GBSA calculations also showed that favipiravir-RMP has a higher binding affinity for HGPRT T138A than for wild-type (Table 3). This is further supported by the observation that, in the bound state, the median values of the average RMSD, its standard deviation, and their minimum values are smaller for HGPRT T138A than for the wild-type and K140M variants (Table 4), indicating relatively reduced structural fluctuations during the simulations. While RMSD does not directly quantify binding affinity, lower fluctuations suggest relatively higher structural stability of the complex, which is consistent with the overall trends from our experimental and energetic analyses. However, despite this relative stability, the maximum values are larger than those in the wild-type, suggesting that HGPRT T138A exhibits greater molecular fluctuations when interactions weaken. This finding supports the interpretation that HGPRT T138A is potentially more prone to releasing favipiravir-RMP than the HGPRT wild-type due to higher overall molecular fluctuation in the bound state. In contrast, for HGPRT K140M, the average RMSD and its standard deviation are consistently larger than those of the wild-type across all statistical measures (minimum, maximum, and median values), indicating relatively less structural stability of the complex and a higher propensity for dissociation, rather than directly implying weaker binding affinity. These findings are consistent with the results of the NMR experiments and ΔG calculations. Furthermore, one of the eight MD trajectories for HGPRT T138A showed the dissociation of favipiravir-RMP from the binding site on the HGPRT while retaining a salt bridge between the favipiravir-RMP and the K140 side chain (Figs. 4D and 5D). The dissociation of favipiravir-RMP from HGPRT might therefore be assisted by conformational flipping of the K140 side chain in a “Lys-anchored escaped state” manner (Figs. 5D and S37). Then, a new interaction is formed between the side chain of R169 residue and the phosphate group of favipiravir, enabling temporary retention of favipiravir-RMP in the binding site of HGPRT until it completely dissociates from HGPRT. Although this was observed in only one MD trajectory, these results are consistent with the NMR result that HGPRT T138A has a higher k_{cat} than wild-type and K140M.

The previously reported X-ray crystallographic analyses suggested that the location of K140 residue allows it to make electrostatic contact with the phosphate group of favipiravir-RMP (Fig. 1). The contribution of K140 residue to the function of HGPRT remains unknown because the electron density of the K140 side chain was not observed, probably due to its high flexibility (Fig. 1). MM-GBSA calculations revealed that the backbone of K140M in HGPRT stabilizes the phosphate group of favipiravir-RMP. Furthermore, MD simulations demonstrated that, in addition to the backbone, the side chain also contributes to the stabilization of the phosphate group, in a manner similar to that observed in the HGPRT wild-type (Figs. 3 and 5). The MD simulations also suggested the involvement of K140 in the dissociation process. The NMR and computational analyses performed in this study provide initial insights into the functional involvement of K140 residue in the HGPRT-catalyzed conversion of favipiravir to favipiravir-RMP.

A previous crystallographic investigation indicated that the backbone amide and carbonyl groups of D193 residue in HGPRT direct contacts the fluorine atom of favipiravir (Fig. 1), although the contribution of the D193 side chain remains unknown[6]. However, a previous study by another group of HGPRT complexed with an inhibitor mimicking the transition state of the HGPRT enzymatic reaction (PDB ID: 1BZY) suggests that D193 residue plays an important role in coordinating a Mg^{2+} ion, essential co-factor for HGPRT and PP*i* association[22]. Substitution of D193 residue to asparagine causes HGPRT to lose its ability to bind Mg^{2+} ion, thereby destabilizing association between HGPRT and *P*Rib-*PP*. It is consistent with our experimental results. Our NMR results not only support the X-ray crystallographic insights but also reveal that the D193-fluorine interaction significantly contributes to the enzymatic conversion of favipiravir to favipiravir-RMP by HGPRT. A previous report further indicated that favipiravir-analogue, F-1105, in which the fluorine atom was replaced with a proton, exhibited no anti-virus activity[6]. In addition, the MD simulation results obtained in this study demonstrated that favipiravir-RMP remained stably bound in the binding site of HGPRT D193N in all eight trajectories (Table 4 and Figures S29–S36). The median RMSD and its standard deviation for D193N were comparable to those of the wild-type, suggesting that the D193N mutation does not substantially impair the overall structural stability of the HGPRT–favipiravir-RMP complex. This observation implies that the loss of Mg^{2+} binding caused by the D193N mutation may affect the catalytic function of HGPRT rather than its capacity to maintain stable binding of favipiravir-RMP. These computational findings suggest that although the D193N mutation may compromise the catalytic function of HGPRT, its ability to sustain ligand binding appears to be structurally preserved.

The NMR approach allowed us to probe the functional hot-spots in HGPRT by estimating various practical enzymatic parameters such as V_{max}, K_m, and k_{cat}. The ^{19}F-NMR experiments measured the quantitative alterations of favipiravir and favipiravir-RMP directly since their NMR signals were adequately separated. Regardless, our results and the previous report of Sugiki et al. (2023) indicate that ^{19}F-based NMR experiments are more advantageous than ^{31}P-observations for accurately characterizing the enzymatic conversion of favipiravir. However, ^{31}P-NMR experiments can provide supportive data on the progress of the enzymatic conversion. The enzymatic parameters V_{max}, K_m, k_{cat} tabulated in Table 2 were estimated from the ^{19}F-NMR data (Figure S3 and Table S1), and could aid in the design of new chemical compounds that are more efficiently metabolized by HGPRT.

Data availability

No datasets were generated or analysed during the current study.

Received: 4 July 2025; Accepted: 5 January 2026

References

1. von Itzstein, M. et al. Rational design of potent sialidase-based inhibitors of influenza virus replication. *Nature* **363**, 418–423. https://doi.org/10.1038/363418a0 (1993).
2. Kim, C. U. et al. Structure-activity relationship studies of novel carbocyclic influenza neuraminidase inhibitors. *J. Med. Chem.* **41**, 2451–2560. https://doi.org/10.1021/jm980162u (1998).
3. Pinto, L. H. & Holsinger, L. J. & Lamb, R. A. Influenza virus M2 protein has ion channel activity. *Cell* **69**, 517–528. https://doi.org/10.1016/0092-8674(92)90452-i (1992).
4. Wang, C., Takeuchi, K., Pinto, L. H. & Lamb, R. A. Ion channel activity of influenza A virus M2 protein: Characterization of the amantadine block. *J. Virol.* **67**, 5585–5594. https://doi.org/10.1128/JVI.67.9.5585-5594.1993 (1993).
5. Furuta, Y. et al. In vitro and in vivo activities of anti-influenza virus compound T-705. *Antimicrob. Agents Chemother.* **46**, 977–981. https://doi.org/10.1128/AAC.46.4.977-981.2002 (2002).
6. Naesens, L. et al. Role of human hypoxanthine guanine phosphoribosyltransferase in activation of the antiviral agent T-705 (favipiravir). *Mol. Pharmacol.* **84**, 615–629. https://doi.org/10.1124/mol.113.087247 (2013).
7. Joshi, S. et al. Role of favipiravir in the treatment of COVID-19. *Int. J. Infect. Dis.* **102**, 501–508. https://doi.org/10.1016/j.ijid.2020.10.069 (2021).
8. Furuta, Y. et al. Mechanism of action of T-705 against influenza virus. *Antimicrob. Agents Chemother.* **49**, 981–986. https://doi.org/10.1128/AAC.49.3.981-986.2005 (2005).
9. Furuta, Y. et al. T-705 (favipiravir) and related compounds: Novel broad-spectrum inhibitors of RNA viral infections. *Antiviral Res.* **82**, 95–102. https://doi.org/10.1016/j.antiviral.2009.02.198 (2009).

10. Furuta, Y., Gowen, B. B., Takahashi, K., Shiraki, K., Smee, D. F. & Barnard, D. L. Favipiravir (T-705), a novel viral RNA polymerase inhibitor. *Antiviral Res.* **100**, 446–454. https://doi.org/10.1016/j.antiviral.2013.09.015 (2013).
11. Peng, Q. et al. Structural Basis of SARS-CoV-2 Polymerase Inhibition by Favipiravir. *Innovation (NY)* 2, 100080. (2021). https://doi.org/10.1016/j.xinn.2021.100080
12. Kaptein, S. J. F. et al. Favipiravir at high doses has potent antiviral activity in SARS-CoV-2-infected hamsters, whereas hydroxychloroquine lacks activity. *Proc. Natl. Acad. Sci. U S A.* **117**, 26955–26965. https://doi.org/10.1073/pnas.2014441117 (2020).
13. Hassanipour, S. et al. The efficacy and safety of favipiravir in treatment of COVID-19: A systematic review and meta-analysis of clinical trials. *Sci. Rep.* **11**, 11022. https://doi.org/10.1038/s41598-021-90551-6 (2021).
14. Shinkai, M. et al. Efficacy and safety of favipiravir in moderate COVID-19 pneumonia patients without oxygen therapy: A Randomized, phase III clinical trial. *Infect. Dis. Ther.* **10**, 2489–2509. https://doi.org/10.1007/s40121-021-00517-4 (2021).
15. Manabe, T., Kambayashi, D., Akatsu, H. & Kudo, K. Favipiravir for the treatment of patients with COVID-19: A systematic review and meta-analysis. *BMC Infect. Dis.* **21**, 489. https://doi.org/10.1186/s12879-021-06164-x (2021).
16. Sugiki, T., Furuita, K., Fujiwara, T. & Kojima, C. Current NMR techniques for structure-based drug discovery. *Molecules* **23**, 148. https://doi.org/10.3390/molecules23010148 (2018).
17. Boeszoermenyi, A. et al. Aromatic ^{19}F-^{13}C TROSY: A background-free approach to probe biomolecular structure, function, and dynamics. *Nat. Methods.* **16**, 333–340. https://doi.org/10.1038/s41592-019-0334-x (2019).
18. Mashiach, R. et al. In situ NMR reveals real-time nanocrystal growth evolution via monomer-attachment or particle-coalescence. *Nat. Commun.* **12**, 229. https://doi.org/10.1038/s41467-020-20512-6 (2021).
19. Sugiki, T. et al. Real-time monitoring of enzyme-catalyzed phosphoribosylation of anti-influenza prodrug favipiravir by time-lapse nuclear magnetic resonance spectroscopy. *NMR Biomed.* **36**, e4888. https://doi.org/10.1002/nbm.4888 (2023).
20. Olp, M. D., Kalous, K. S. & Smith, B. C. ICEKAT: An interactive online tool for calculating initial rates from continuous enzyme kinetic traces. *BMC Bioinform.* **21**, 186. https://doi.org/10.1186/s12859-020-3513-y (2020).
21. Xu, Y., Eads, J., Sacchettini, J. C. & Grubmeyer, C. Kinetic mechanism of human hypoxanthine-guanine phosphoribosyltransferase: Rapid phosphoribosyl transfer chemistry. *Biochemistry* **36**, 3700–3712. https://doi.org/10.1021/bi9616007 (1997).
22. Keough, D. T., Brereton, I. M., de Jersey, J. & Guddat, L. W. The crystal structure of free human hypoxanthine-guanine phosphoribosyltransferase reveals extensive conformational plasticity throughout the catalytic cycle. *J. Mol. Biol.* **351**, 170–181. https://doi.org/10.1016/j.jmb.2005.05.061 (2005).
23. Eastman, P. et al. OpenMM 7: Rapid development of high performance algorithms for molecular dynamics. *PLoS Comput. Biol.* **13**, e1005659. https://doi.org/10.1371/journal.pcbi.1005659 (2017).
24. Schrödinger, L. L. C. *The PyMOL Molecular Graphics System, Version 2.5, Schrödinger* (LLC, 2021).
25. Sastry, G. M., Adzhigirey, M., Day, T., Annabhimoju, R. & Sherman, W. Protein and ligand preparation: Parameters, protocols, and influence on virtual screening enrichments. *J. Comput. Aided Mol. Des.* **27**, 221–234. https://doi.org/10.1007/s10822-013-9644-8 (2013).
26. Schrödinger, R., Epik, Schrödinger, L. L. C., New York, N. Y., Impact & Prime Protein Preparation Wizard;, 2023;Schrödinger, LLC, New York, NY; Schrödinger, LLC, New York, NY (2023). (2023)-4.
27. Jacobson, M. P., Friesner, R. A., Xiang, Z. & Honig, B. On the role of the crystal environment in determining protein side-chain conformations. *J. Mol. Biol.* **320**, 597–608. https://doi.org/10.1016/s0022-2836(02)00470-9 (2002).
28. Jacobson, M. P. et al. A hierarchical approach to all-atom protein loop prediction. *Proteins* **55**, 351–367. https://doi.org/10.1002/prot.10613 (2004).
29. Schrödinger *Release 2023-4: Prime, Schrödinger* (LLC, 2023).
30. Bowers, K. J. et al. Scalable algorithms for molecular dynamics simulations on commodity clusters, *Proc. ACM/IEEE Conf. Supercomput. (SC06)* Tampa, Florida, November 11–17 (2006).
31. Schrödinger Release 2019-1: Desmond Molecular Dynamics System, Shaw, D. E. & Research New York, NY, Maestro-Desmond Interoperability Tools, Schrödinger, New York, NY (2019). (2019).
32. Gowers, R. J. et al. MDAnalysis: A Python package for the rapid analysis of molecular dynamics simulations. In *Proceedings of the 15th Python in Science Conference* 98–105. (2016). https://doi.org/10.25080/majora-629e541a-00e
33. Michaud-Agrawal, N., Denning, E. J., Woolf, T. B. & Beckstein, O. MDAnalysis: A toolkit for the analysis of molecular dynamics simulations. *J. Comput. Chem.* **32**, 2319–2327. https://doi.org/10.1002/jcc.21787 (2011).
34. Takahashi, R. et al. Structure and reaction mechanism of human nicotinamide phosphoribosyltransferase. *J. Biochem.* **147**, 95–107. https://doi.org/10.1093/jb/mvp152 (2010).
35. Escobedo-Hinojosa, W., Wissner, J. L. & Hauer, B. A real-time ^{31}P-NMR-based approach for the assessment of glycerol kinase catalyzed monophosphorylations. *MethodsX* **8**, 101285. https://doi.org/10.1016/j.mex.2021.101285 (2021).
36. Smithers, G. W. & O'Sullivan, W. J. ^{31}P nuclear magnetic resonance study of phosphoribosyldiphosphate and its interaction with magnesium ions. *J. Biol. Chem.* **257**, 6164–6170. https://doi.org/10.1016/S0021-9258(29)65121-3 (1982).

Acknowledgements

We would like to express our gratitude to Prof. Tetsuya Suhara and Dr. Kumiko Saegusa (QST, Japan), Prof. Munehiro Inukai (Tokushima University, Japan), and Prof. Shinsuke Sando (The University of Tokyo, Japan) for many discussions and suggestions.

Author contributions

All authors made substantial contributions to the following; the conception and design of this work were performed by T.S., T.Y., M.T., K.M., A.K., T.F., and M.N.; sample preparation and the acquisition of NMR data and its analyses were performed by T.S.; the acquisition and analyses of computational calculation and MD simulation data were performed by T.Y. and N.T.; the drafting this article and revisions were performed by all the authors, T.S., T.Y., M.T., K.M., A.K., N.M., T.U., J.F., Y.H., T.M., T.F., M.K., Y.M., K. S-K., Y.T., N.T., and M.N.; and final approval of submission of this manuscript was by T.S.

Funding

This work was financially supported by the Frontier Science Support Program by the Institute for Protein Research (Grant Number R1-2), the CASIO SCIENCE PROMOTION FOUNDATION (Grant Number J41-42) funds, JSPS KAKENHI (Grant Numbers JP21K06046 and JP23K05654), CREST (Grant Number JPMJCR1672) from JST, the Platform Project for Supporting Drug Discovery and Life Science Research (Basis for Supporting Innovative Drug Discovery and Life Science Research (BINDS)) Grant Number JP20am0101072 from AMED, and MEXT Quantum Leap Flagship Program (MEXT Q-LEAP) Grant Number JPMXS0120330644 and World Premier International Research Center Initiative (WPI) from JST.

Declarations

Competing interests

The authors declare no competing interests.

Additional information

Supplementary Information The online version contains supplementary material available at https://doi.org/10.1038/s41598-026-35354-3.

Correspondence and requests for materials should be addressed to T.S.

Reprints and permissions information is available at www.nature.com/reprints.